

IMPURITY LEAKAGE AND RADIATIVE COOLING IN THE FIRST NITROGEN AND NEON SEEDING STUDY IN THE SLOT DIVERTOR AT DIII-D

L. Casali^{1,2}, D. Eldon¹, A. McLean³, T. Osborne¹, A. Leonard¹, B. Grierson⁴, J. Ren¹

¹ *University of Tennessee-Knoxville, Knoxville, Tennessee, USA*

² *General Atomics, San Diego, CA, USA*

³ *Lawrence Livermore National Laboratory, Livermore, USA*

⁴ *Princeton Plasma Physics Laboratory, Princeton, New Jersey, USA*

Abstract

A comparative study of nitrogen versus neon has been carried out to analyze the impact of the two radiative species on power dissipation, SOL impurity distribution, divertor and pedestal characteristics. The experimental results show that N remains compressed in the divertor, thereby providing high radiative losses without affecting the pedestal profiles and displacing carbon as dominant radiator. Neon, instead, radiates more upstream than N thus reducing the power flux through the separatrix leading to a reduced ELM frequency and compression in the divertor. A significant amount of neon is measured in the plasma core leading to a steeper density gradient. The different behaviour between the two impurities is confirmed by SOLPS-ITER modelling which for the first time at DIII-D includes multiple impurity species and a treatment of full drifts, currents and neutral-neutral collisions. The impurity transport in the SOL is studied in terms of the parallel momentum balance showing that N is mostly retained in the divertor whereas Ne leaks out consistent with its higher ionization potential and longer mean free path. This is also in agreement with the enrichment factor calculations which indicate lower divertor enrichment for neon. The strong ionization source characterizing the SAS divertor causes a reversal of the main ions and impurity flows. The flow reversal together with plasma drifts and the effect of the thermal force contribute significantly in the shift of the impurity stagnation point affecting impurity leakage. This work provides a demonstration of the impurity leakage mechanism in a closed divertor structure and the consequent impact on pedestal. Since carbon is an intrinsic radiator at DIII-D, in this paper we have also demonstrated the different role of carbon in the N vs Ne seeded cases both in the experiments and in the numerical modeling. Carbon contributes more when neon seeding is injected compared to when nitrogen is used. Finally, the results highlight the importance of accompanying experimental studies with numerical modelling of plasma flows, drifts and ionization profile to determine the details of the SOL impurity transport as the latter may vary with changes in divertor regime and geometry. In the cases presented here, plasma drifts and flow reversal caused by high level of closure in the slot upper divertor at DIII-D play an important role in the underlined mechanism.

1. INTRODUCTION

High heat and particle fluxes at plasma facing components (PFC) are a major issue for the design and operation of next step fusion devices because they can damage wall materials and lead to impurity influx into the plasma, which deteriorates performance due to enhanced radiation losses and fuel dilution. A well-established technique to reduce heat loads on divertor target plates is to insert low and medium Z impurities in the plasma to convert the heat flux into electromagnetic radiation and redistribute it over the whole plasma vessel surface. Impurity seeding is already required in present W machines due to the absence of the carbon as intrinsic radiator and it will be mandatory in ITER and future reactors with a W divertor to reduce power loads on divertor components and reduce erosion [1].

Impurity radiation is the main drive of the energy dissipation processes [2] enabling the temperature reduction to $\sim 5\text{eV}$ where the ion-neutral interaction zone becomes important. At this stage, charge exchange and elastic collisions reduce the temperature down to $\sim 1\text{ eV}$ where recombination is initiated and divertor detachment, a cold dissipative divertor with reduced heat and particle flux, is obtained. To this end, impurity screening in the divertor is important not only to promote divertor detachment but also to confine the impurity in the divertor volume in order to not contaminate the core plasma. It has been demonstrated that a closed divertor structure enhances neutral compression and can achieve detachment at lower upstream density which is favourable for core-edge integration [3, 4, 5, 6, 7, 8, 9]. For a given divertor configuration, the choice of the impurity seeding is important: nitrogen is an excellent divertor radiator in present machines which enables the reduction of target heat flux with unchanged or even improved confinement [10, 11, 12, 13]. However, due to ammonia formation, the use of nitrogen may pose a problem for ITER operation and therefore neon is discussed as a replacement seeding gas in power exhaust application since it is chemically inert and radiates at temperatures relevant for ITER and future reactors [14, 15]. The international community is undertaking a significant effort to assess the effects of neon seeding as a suitable radiator for both divertor and pedestal conditions. Here, we contribute to such effort by comparing nitrogen and neon seeding in the Small Angle Slot (SAS) slot divertor at DIII-D. The upper single null SAS configuration combines a gas-tight slot geometry with a small target angle to maximize the power and momentum dissipation of recycling neutrals [16, 17]. This work focuses on the comparison of nitrogen and neon as seeding gases keeping fixed the divertor geometry and investigating their effect on both divertor and pedestal performance.

2. NITROGEN AND NEON SEEDING EXPERIMENTS

A detailed study comparing the effect of nitrogen and neon on power dissipation and pedestal performance has been carried out using the SAS slot divertor located in the upper divertor of the DIII-D tokamak (fig.1a). This study has been enabled by unprecedented diagnostic coverage in a closed divertor which enabled multiple independent observations of plasma cooling evolution. The suite of boundary diagnostics which is shown in fig.1b includes: Langmuir probes (LPs), in-tile pressure gauges (PGs), Surface Eroding Thermocouples (SETCs), the divertor Thomson scattering (DTS) system with three channels along the vertical viewing chord passing through the slot, as well as the ultraviolet wavelength spectrometer (DivSPRED) and the near infrared spectrometer (NIRS). The work presented here is based on

experiments where the gas species was varied and the outer strike point (OSP) was kept at the inner surface which in L. Casali et al. [18] was identified to be the optimal location for impurity retention. In [18] it was demonstrated that for identical discharges, higher level of relative nitrogen contamination was consistently measured in the core when the outer strike point was located at the outer corner of the slot compared to when the strike point was positioned on the inner slanted target. Additionally, the detachment onset required higher nitrogen puff when the OSP was located at the outer corner compared to the inner corner. Following these important results, the experiments presented here, which aimed to compare nitrogen versus neon behavior as radiative species, were performed keeping the OSP at the inboard side (fig.1)

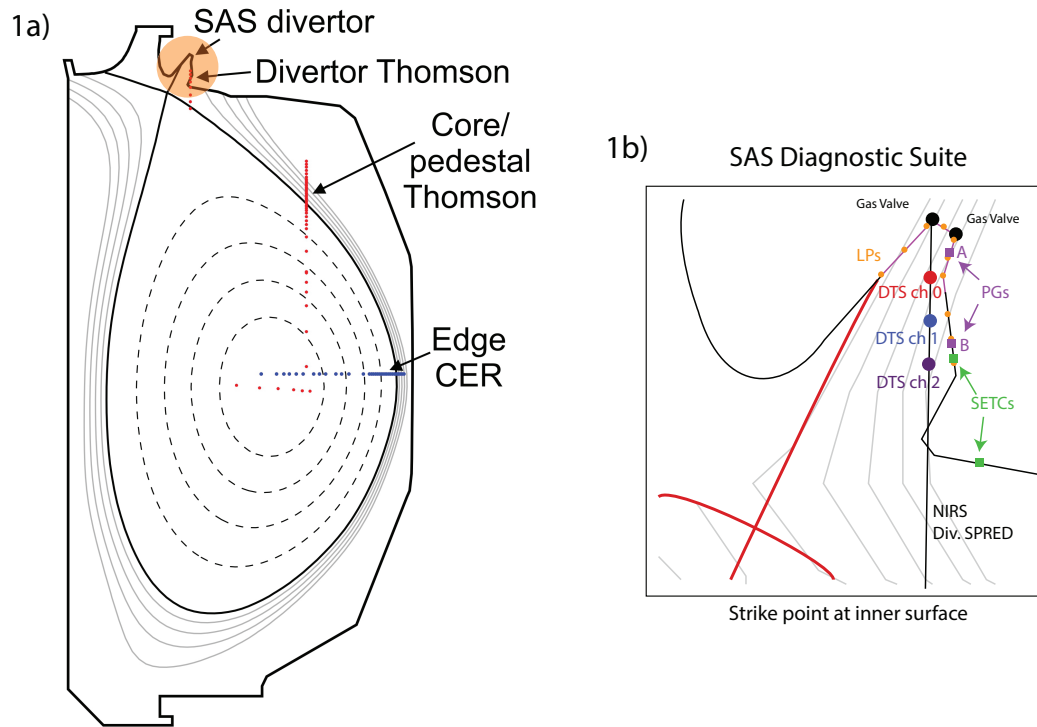


Figure 1a: Full poloidal cross-section of DIII-D, the SAS slot divertor located in the upper divertor is highlighted in orange. Fig. 1b shows the SAS divertor with its comprehensive set of boundary diagnostics. In the studies shown here, the strike point (in red) is located at the inner slanted surface.

The experiments were performed in H-mode with $I_p = 1.0$ MA, $B_t = 2$ T with ion $B \times \nabla B$ directed into the SAS (toward the X-point in the upper divertor), $P_{NBI} = 4.5$ and 8 MW with related density scans. Impurities were injected through two independent in-slot gas valves located at the inner and at the outer corner of the slot (black circles in Fig. 1b) using the same flow rate from each valve. The two valves are located at the same poloidal location but at two different toroidal locations, hence toroidal symmetry is assumed in the interpretation of the data. The discharges were performed keeping fixed the input parameters such as I_p , B_t , input power (fig. 2) and comparing nitrogen versus neon seeding to isolate the effect of the radiative species. In order to obtain a similar radiation fraction for the two impurities (fig. 2b and 2h), a lower flow rate was required for Ne (fig. 2i) compared to N (fig. 2c) due to the higher radiation efficiency and the higher recycling for neon. At 4.5s nitrogen puff was increased to trigger more pronounced detachment. The surface eroding thermocouples which measure the surface temperature indicate a reduction of the heat flux (fig. 2e and 2k) during

the seeding phase with both impurities although more pronounced in the nitrogen case. Note that the SETC measurements are taken in the far SOL on the other side of the slot compared to the strike point location which is located on the inboard surface (fig.1). The fact that the SETC detects such reduction of the heat flux when the impurities are injected despite the diagnostic being well far away from the strike point implies that the plasma cooling is not a localized phenomenon but it extends through the entire slot.

For otherwise identical input parameters in discharges comparing nitrogen versus neon seeding, it was found that neon increases the radiation profile in the core compared to nitrogen (fig. 3b). The increased core radiation with neon (fig. 3b) is consistent with the fact that neon radiates at higher T_e than nitrogen as indicated by the radiative loss factors as function of T_e shown for the two seeded impurities (fig. 3a). The neon radiative mantle leads to a decrease of the power flux through the separatrix reducing the power available for ionization in the Scrape Off Layer (SOL) and divertor. Because of this lower upstream power flux, there is less power to be dissipated downstream and the compression capability of the divertor is reduced as demonstrated by the lower neutral pressure in the slot with neon seeding as measured by an in-tail pressure gauge (fig. 2j). Another consequence of the neon radiating mantle is a dramatic reduction in the ELM frequency which can be seen in the $D\alpha$ signal in fig. 2l) as measured by the filterscope SAS chord at 30 degree. When neon is in the plasma, less frequent and larger ELMs appear with a quiescent period with no small ELMs in between the bigger ones. This is an important observation because the lack of frequent ELMs implies a reduced ability to expel impurities back in the SOL which favors impurity build up in the pedestal. This mechanism is the reason why the operational window with Ne seeding is very narrow in medium size tungsten machines and often leads to radiation collapse [19].

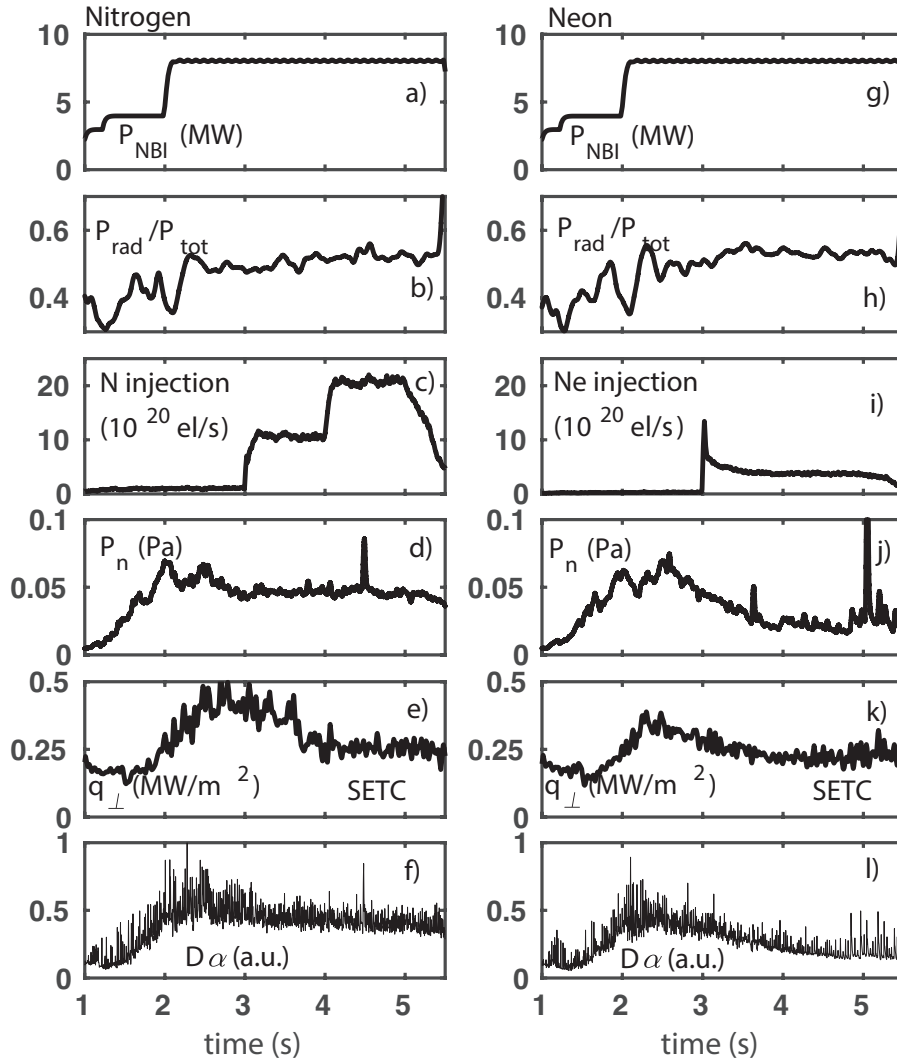


Figure 2: (a) NBI power, (b) radiation fraction, (c) impurity gas puff rate, (d) neutral pressure from in-slot pressure gauge PG_A, (e) q_{\perp} from SETC, (f) $D\alpha$ from filterscope for the nitrogen seeded case. (g) NBI power, (h) radiation fraction, (i) impurity gas puff rate, (j) neutral pressure from in-slot pressure gauge PG_A, (k) q_{\perp} from SETC, (l) $D\alpha$ from filterscope for the neon seeded case.

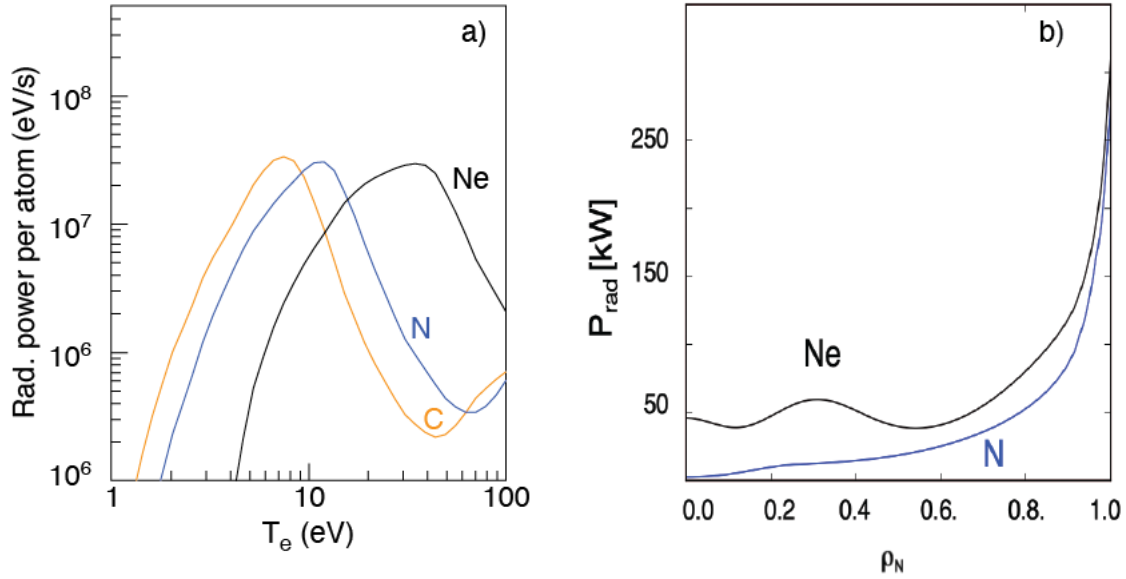


Fig.3: a) Radiative loss factors as function of T_e for carbon (orange), nitrogen (blue) and neon (black). b) Radiation profile for the seeded impurities nitrogen (blue) and neon (black).

The impact of the two impurities in the divertor has been further evaluated using an extreme/vacuum ultraviolet (EUV/VUV) spectrometer which monitors the dominant radiant emissions for low and medium-Z elements, including resonance lines – those connected directly to the ground state. Because the majority of the radiation from the plasma is emitted in the divertor region and in particular in the EUV/VUV region, this spectral measurement is a good approximation of the total radiated power from the plasma. This spectrometer – the Divertor SPRED (DivSPRED) – has a vertical view through the outer strike point (OSP) and SOL of the divertor and region beyond the X-point. Figure 4 shows spectra for the neon seeded discharge (fig. 4a) and the nitrogen seeded discharge (fig. 4b). The spectra are taken both before the impurity puff begins, and subsequently during the puff well after the gas rate and plasma have had time to equilibrate. A difference of the spectra during gas puff and spectra before gas puff is then taken to reveal the incremental impact of the gas puff on the plasma alone. For the Ne injection, the perturbation to the radiation along the line of sight in the SOL impacts higher charge states almost exclusively. For Ne itself, additive emission from Ne IV, V, VI, VII, VIII, and IX is present in the spectrum in the 55-100 nm range. This suggests that the neon is accumulating in regions where the electron population is sufficiently hot to ionize Ne as high as the +8 charge state; this implies $T_e > 100$ eV, which occurs only well upstream of the targets. The increase in radiated power which leads to the onset of cold conditions in the divertor plasma is happening closer to the X-point and to the outer target separatrix with neon injection.

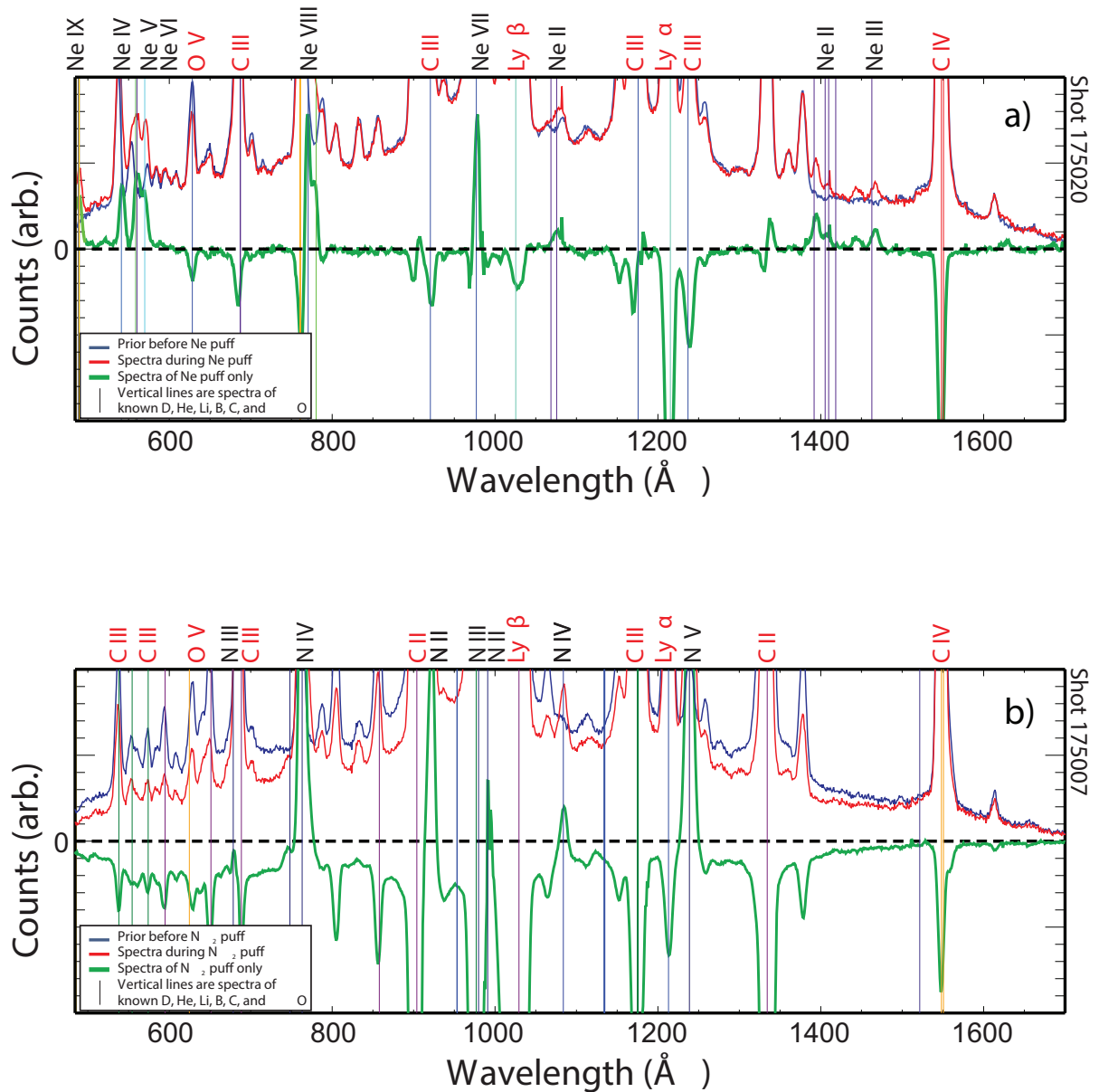


Figure 4: Spectral measurements from the EUV/VUV spectrometer Divertor SPRED for a) the neon discharge, b) nitrogen discharge before the impurity puff (in blue), during the impurity puff (red), difference of spectra between pre-puff and post-puff of N or Ne impurities (in green).

For comparison, the spectrum of the nitrogen discharge is shown in figure 4b. Here prominent new lines from NII, III, IV, and V appear in the spectrum, consistent with resonance emissions from N ions, however a comprehensive reduction in C emissions is now present. CII and CIII emissions drop by $\sim 50\%$, while C IV, 155 nm reduces by $\sim 25\%$. This might suggest a different dynamic for N compared to Ne, where N is displacing the C as the dominant radiator in agreement with Ref [20]. This radiation displacement of N by C is interesting because it suggests a feedback mechanism is at play where the injected N is found to supplant the intrinsic C emission along the line of sight observed by the DivSPRED diagnostic along the outer SOL. The presented measurements indicate that nitrogen is taking over the dissipation carbon was doing whereas neon is radiating in a different T_e range upstream.

The different nitrogen and neon dissipative behavior inferred by these detailed experimental data has been confirmed by numerical analysis using the SOLPS-ITER code as presented in the next section. The experimental profile analysis indicates that a higher amount of neon is measured in the core compared to nitrogen (fig. 5). Fig. 5a shows the electron density and the impurity density for the nitrogen seeded discharge. Fig. 5b shows the electron density and the impurity density for the neon case. The profiles before the seeding are depicted in solid line while the profiles during the seeding are shown in dashed. In the nitrogen discharge, the electron density is hardly changed compared to the non-seeding phase and a very low level of nitrogen density is measured by CER in the confined region (fig. 5a). With neon, instead, the electron density profile steepens and a large neon density is measured in the core (fig. 5b). For reference, the carbon profiles in both cases are also plotted. In the N discharge, the carbon impurity profile remains well above the carbon one; instead in the Ne discharge, the neon density is higher than the carbon density.

The results shown here indicate that the two routes for power dissipation using N through divertor radiation and Ne through radiating mantle upstream lead to different pedestal responses where the latter are fundamentally linked to the impurity distribution and transport in the SOL which is analyzed below.

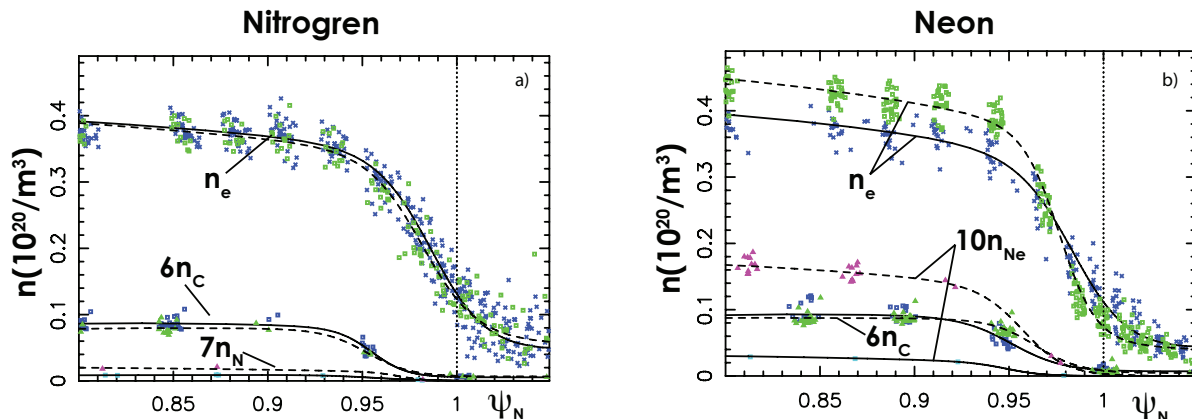


Figure 5: Experimental density profiles for a) the nitrogen seeding discharge and b) for the neon seeding discharge. The blue points are the experimental data taken before the impurity seeding starts (with corresponding fit in solid line), while the green points are the experimental data during the impurity seeding (with corresponding fit in dashed line). The total carbon density profiles n_c is also shown for comparison.

3. SOL IMPURITY DISTRIBUTION AND TRANSPORT WITH SOLPS-ITER

3.1 MODELING SETUP

To interpret these interesting experimental results, the SOLPS-ITER code [21] has been used to study the SOL impurity transport and determine the impurity compression in the nitrogen and neon case. The SOLPS-ITER code couples the B2.5 multi-fluid plasma code and EIRENE Monte Carlo neutral transport code. Electrons and ions are treated by the fluid code, which provides the background plasma on which the neutral trajectories are computed. The neutrals are tracked by EIRENE, which takes into account detailed atomic processes such as ionization, volume recombination, charge exchange, and elastic collisions. For the first time,

SOLPS-ITER simulations with D+C+N/Ne, all drifts, currents and n-n collisions activated are performed at DIII-D. In this work, the SOLPS-ITER version [22] was used which includes the most accurate form of the impurity force balance at arbitrary concentrations based on kinetic calculations. At the core boundary, the input power is equally split between electrons and ions and such to match the power crossing the separatrix. At the target, sheath conditions are applied according to the standard Bohm criterion with $v \geq c_s$. Leakage-type boundary conditions are used at the Scrape Off Layer (SOL) and at the Private Flux Region (PFR), with the ion leakage in the outer boundary given by $\Gamma_{\text{loss}} = \alpha c_s n_p$ where c_s is the sound speed, n_p the particle density and α the leakage factor usually assumed to be equal to 0.001. The leakage flux magnitude is aligned with SOLPS-ITER modeling of DIII-D plasmas [23,18]. The species included in the simulations are D^0 , D_2 , D^+ , D_2^+ and all ionization states of carbon, nitrogen and neon. As in the experiments, nitrogen (or neon) is puffed by the two gas valves situated at the two corners of the SAS slot as shown in fig. 1. Nitrogen seeding is simulated by an influx of atomic N, hence nitrogen chemistry as well as associated release mechanisms (CN) are not taken into account. These effects are an active area of research [24]. Carbon is produced by chemical and physical sputtering due to deuterium ions and neutrals. The total recycling rate for D is fixed to $R = 1$ at the target and to 99.8% for all the other surfaces. Ions recycle back into the simulation domain as fast neutral D atoms by reflection and D_2 by thermal release. The probability of reflection p_f is calculated by the Monte Carlo TRIM model [25] while the thermal release probability is given by $p_t = R - p_f$. Neutrals penetrating inside the innermost flux surface are assumed to return as fully stripped ions. The carbon chemical sputtering yield is fixed at 2%, whereas the physical sputtering yield is derived using the modified Roth–Bohdansky formula [26]. Carbon is considered a sticky impurity so the carbon ion/neutral flux is not recycled, i.e. $R = 0$. The real magnetic geometry from the EFIT equilibrium fitting code is used. The anomalous transport coefficients are such that the computed profiles match as best as possible the experimentally measured upstream profiles just before the impurity seeding was applied (fig. 6). The transport coefficients were set spatially constant with $\chi = 1 \text{ m}^2/\text{s}$ (with $D = 0.3 * \chi$) which value drops to $\chi = 0.2 \text{ m}^2/\text{s}$ to reproduce the H-mode transport barrier. In the divertor and in the private flux region, the diffusivities are increased by a factor of 10 to represent divertor turbulence and provide divertor particle and heat flux spreading roughly consistent with DIII-D results [23]. Since the main point of this work is to assess the use of different seeding gases and their impact on divertor and pedestal conditions, all input parameters are kept equal, and only the seeded species is varied, allowing us to isolate the effect of N vs Ne as radiative impurities. The model for drifts includes the treatment of $E \times B$ drift, ∇B drift, viscosity, electrical potential and the associated currents. As in the experiments, the ion $B \times \nabla B$ is directed into the divertor, which means that poloidal cross-field drifts are in the counterclockwise direction and tend to redistribute particles from the outer to the inner divertor.

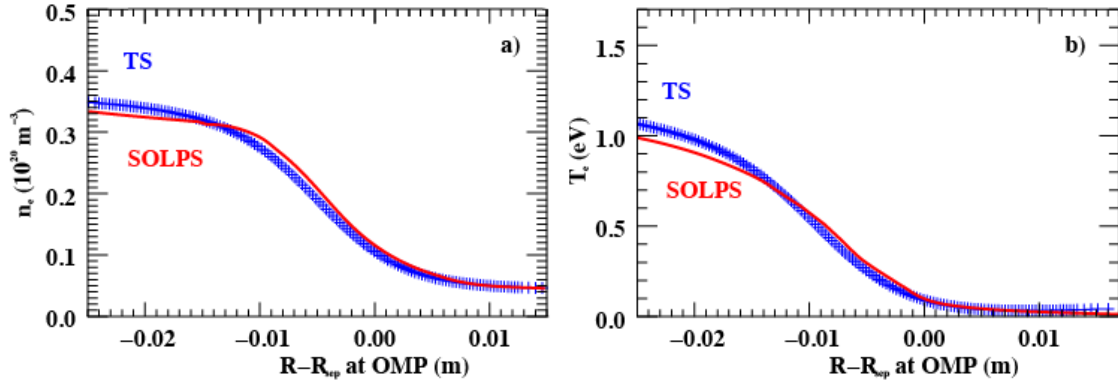


Fig.6: Upstream Profiles of a) electron density, b) electron temperature measurements from Thomson scattering TS (blue) and from SOLPS (red).

3.2 IMPURITY DISTRIBUTION AND RADIATIVE COOLING

The modeling results indicate that for a very similar plasma background, nitrogen and neon distributions are very different. Fig. 7 shows the 2D contour plot of the impurity distribution for the nitrogen seeded discharge (fig. 7a) and the neon seeded case (fig. 7b). Fig. 8a and 8b illustrate the 2D contour plots of the electron temperature for the nitrogen seeded discharge and for the neon seeded case respectively. The comparison demonstrates that nitrogen is localized in the region of low temperature close to the target, while neon doesn't form a density peak at the target but it leaks out of the divertor, reaching the upstream plasma where it radiates consistent with the experimental findings shown in fig.4 and fig.5. With ion $B \times \nabla B$ into the SAS, cross field poloidal drifts induce transport from the outer to the inner divertor through the private flux region (PFR) leading to high enrichment of the impurities at the inner target at the inner wall as can be seen in fig.7. Ref [18] presented results for a nitrogen case with and without drifts showing the enrichment at the inner target with drifts activated and an increased flow to the outer target and a reduction in T_e when drifts were deactivated. Additionally, the amplitude of $E \times B$ drift flows in the SAS is found to be of the same order of magnitude as the recycling plasma flows. This means that drifts play an important role in determining the impurity distribution and overall SOL transport [18, 27] demonstrating the importance of including drifts in the cases studied in this work.

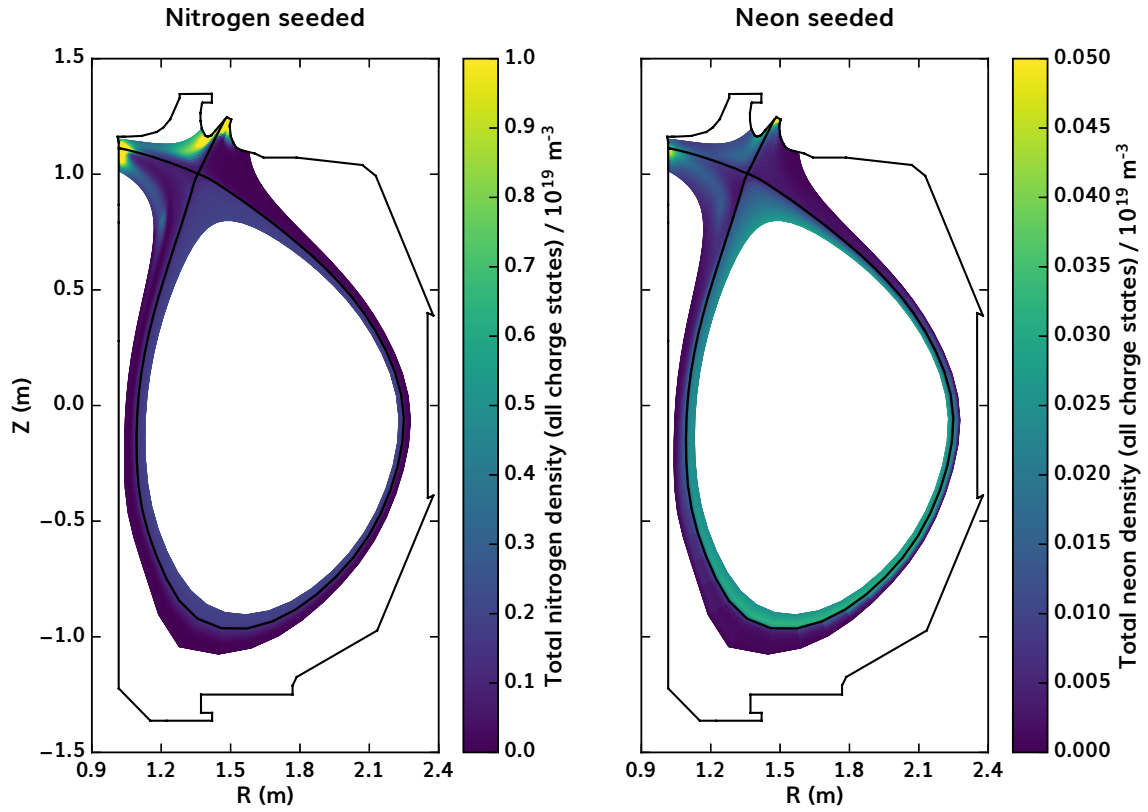


Figure 7: a) N impurity density, b) Ne impurity density. N is localized in the region of very low temperature at the target (see fig. 8a). Ne is not localized at the target but instead penetrates upstream.

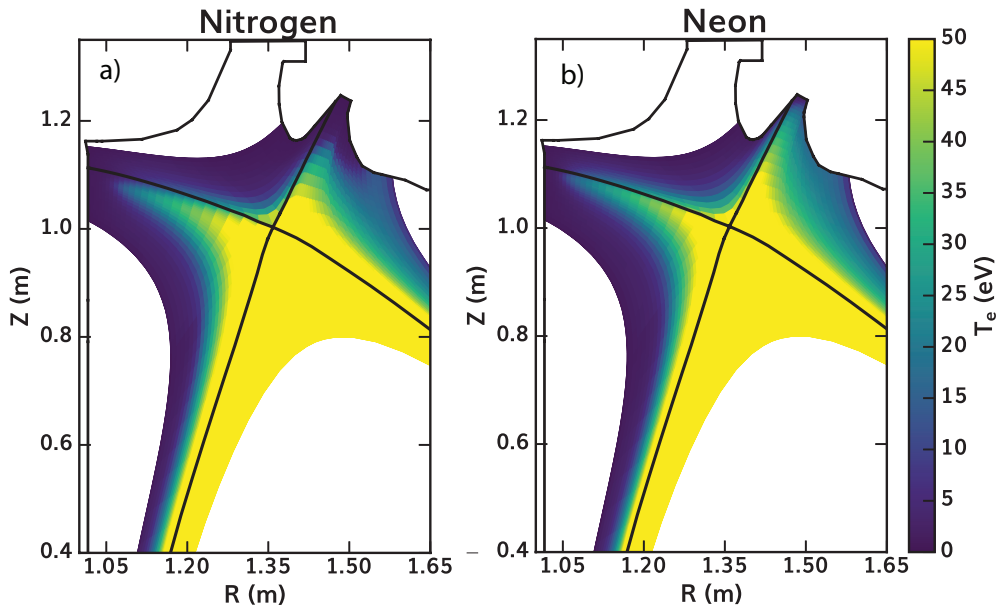


Figure 8: a) T_e in the nitrogen seeded case, b) T_e in the neon seeded case.

The obtained result that nitrogen remains localized in the divertor while neon penetrates upstream has important implications because the choice between neon and nitrogen as seeded species depends on where these gases radiate and on their radiative efficiency as function of the temperature as shown in fig. 3 in agreement with [1, 28].

The fact that neon dissipates more upstream than nitrogen can be further demonstrated by looking at the parallel heat flux at the divertor entrance as calculated by SOLPS-ITER (fig. 9): q_{\parallel} at the X-point is 2x lower in the case of Ne compared to N indicating that neon is radiating more power upstream than the nitrogen so less heat arrives at the divertor. This is also in consistent with the experimental results shown in fig.5 that higher amount of neon is measured in the core compared to nitrogen.

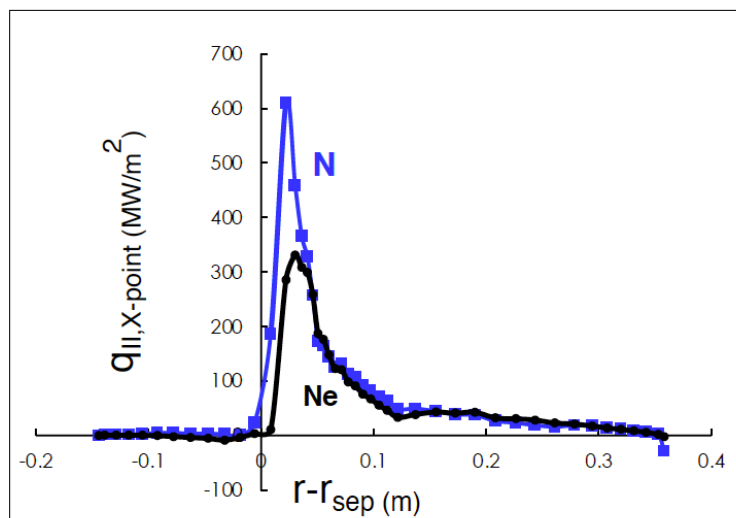


Figure 9: Parallel heat flux at the X-point (entrance to the divertor) from SOLPS-ITER modelling in blue for nitrogen and in black for Ne.

In addition to nitrogen and neon which were seeded as extrinsic radiators, carbon is an intrinsic radiator in DIII-D and it is of interest to look at the role of carbon in the two different cases with nitrogen and neon seeding. Fig. 10 illustrates the radiation fraction due to carbon showing that carbon has a larger role to play in the neon-seeded case. Carbon contributes more when neon seeding is used compared to when nitrogen is injected. This can be understood considering that the radiation profile between nitrogen and carbon is very similar (see fig.3). Neon instead radiates at higher temperature, more upstream, which implies that at lower temperature down near the target the fraction is dominated by carbon radiation. This is qualitatively consistent with the experimental results from DivSPRED which detects a lower emission from carbon in the nitrogen case compared to the neon discharge.

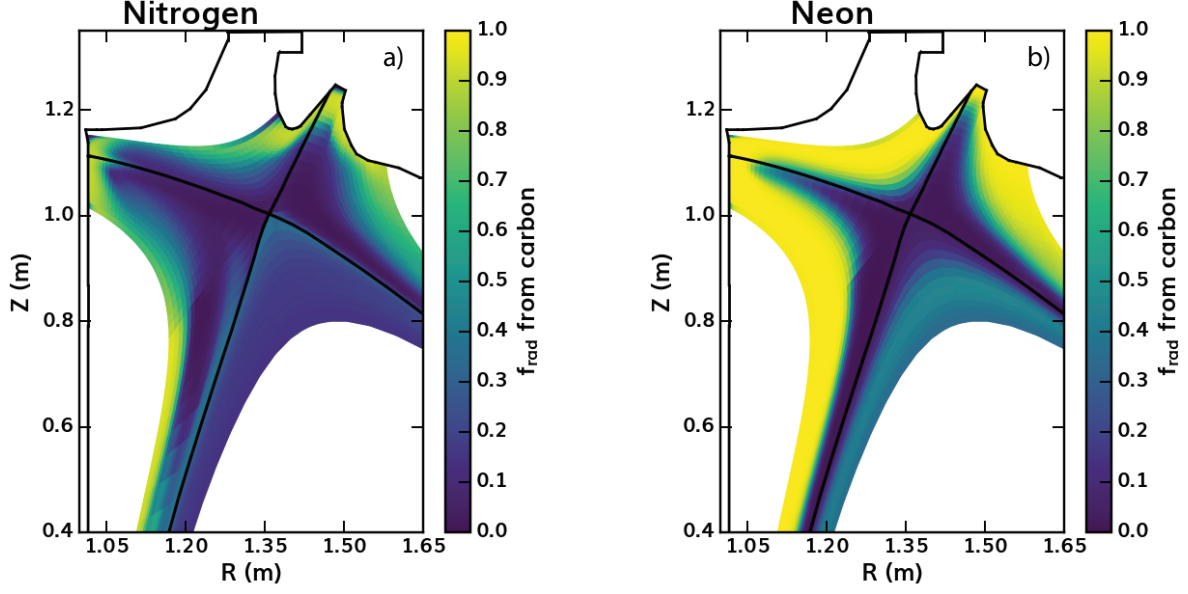


Figure 10: Radiation fraction due to carbon in a) nitrogen seeded case, b) neon seeded case.

3.2 MOMENTUM BALANCE ANALYSIS AND IMPURITY LEAKAGE

In addition to determining the divertor target power asymmetries and the transition to detachment, the redistribution of impurities in the SOL plays a crucial role in determining impurity divertor leakage and consequent core impurity accumulation with significant implication for pedestal behaviour and core performance. To this end, we analyze the impurity density and the momentum balance for the two radiative species with the SOLPS-ITER code. The impurity distribution is the result of the parallel force balance which in the stationary form can be written as [29, 30]:

$$-\nabla_{\parallel} n_i T_i + S_{i,fr} + S_{i,th} - eZn_i \nabla_{\parallel} \phi = 0 \quad [1]$$

Where $-\nabla_{\parallel} n_i T_i$ represents the pressure gradient, $S_{i,fr}$ is the friction force due to the main ions, $S_{i,th}$ is the thermal force and $eZn_i \nabla_{\parallel} \phi$ the electric force.

The force balance determines the difference between the parallel velocity of the main ions and impurity ions. For the latter, the distribution tends to be flat in the SOL but pronounced in the divertor to balance the pressure drop below the ionization point and the reduction in T_e at the target. An example of the parallel momentum balance for our SAS cases is illustrated in fig. 11 for N (fig. 11a) and Ne (fig. 11b). The calculated momentum balance takes into account all the terms contributing to the impurity force balance equation including ionization, recombination, viscosity and inertia. In figs. 11a and 11b the forces are summed over all nitrogen and neon ionization states excluding neutrals. The momentum balance indicates that the dominant forces are the thermal (in green) and the friction (in blue) forces with the main ions. The electric forces (in red) and the impurity pressure gradients (in cyan) have only a minor contribution. The small contribution of the impurity pressure gradient (see cyan line in

fig. 11a and 11b) indicates that the parallel diffusion of the impurity compared to the main ions is not significant. Note that the force balance changes moving from the outer to the inner target.

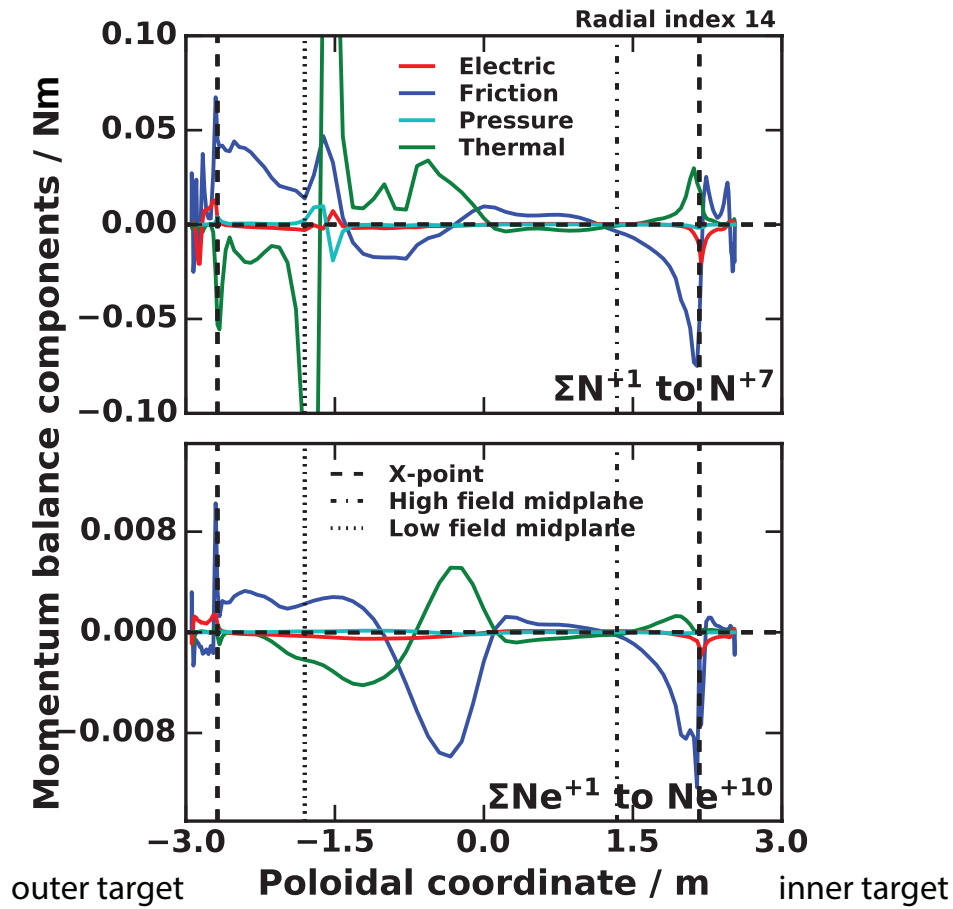


Figure 11: Parallel momentum balance: a) for the N discharge, b) for the Ne discharge. The momentum balance is calculated on the flux tube just outside from the separatrix at outer midplane. The forces are summed over all the impurity ionization states excluding neutrals.

From the momentum balance, the expression for the impurity parallel velocity can be determined. The impurity parallel velocity depends on the main ion velocity $v_{||,i}$ through the friction force and a term that depends on the parallel projection of the main ion temperature gradient $\nabla_{||}T_i$ with m_i the impurity ion mass, τ the collision time, α and β numerical coefficients:

$$v_{||,I} \cong v_{||,i} + \frac{\beta}{\alpha} \tau \frac{1}{m_i} \nabla_{||} T_i \quad [2]$$

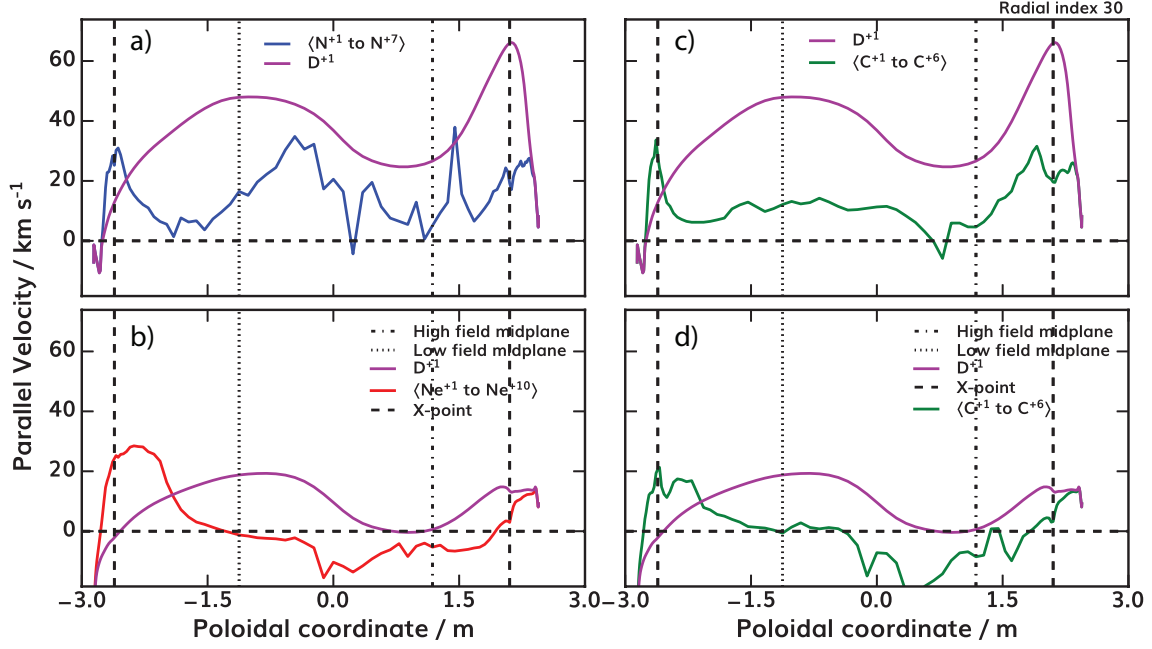


Figure 12: a) Parallel velocity of D+1 (magenta) and N+1 to N+7 (in blue), b) Parallel velocity of D+1 (magenta) and Ne+1 to Ne+10 (red), c) Parallel velocity of D+1 (magenta) and C+1 to C+6 (in green) in the nitrogen seeded case, c) d) Parallel velocity of D+1 (magenta) and C+1 to C+6 (in green) in the neon seeded case.

The impurity velocities for nitrogen, neon and main ions are plotted in fig. 12a and 12b. The comparison of these velocities indicates that in the cases considered in this work, there are regions where there is a large difference between the velocity of the main ions (in magenta) and the velocity of the impurities (in blue for nitrogen, in red for neon). This is due to the thermal force produced by the ion temperature gradient. Since the ion temperature gradient is directed upstream, the effect of the thermal force is a shift in the impurity stagnation point (the point where $v_{||,I} = 0$) towards the target with respect to the stagnation point of the main ion parallel velocity. Hence, it becomes more likely for impurities to reach the stagnation point before they are ionized and therefore more likely to leak out of the divertor. These zones with large difference between the parallel velocity of the impurity and the main ions correspond to the zones in figs. 11a and 11b where the friction force between main ions and impurities is balanced by the thermal force. A similar dynamic is found for the interplay between carbon ions and main ions (fig. 12 b and d).

The stagnation point might be shifted by the plasma drifts and therefore the ultimate quantity describing the impurity transport in the SOL is the impurity poloidal velocity v_{pol} . The impurity poloidal velocity depends on the poloidal projection of the parallel impurity velocity and the poloidal velocity due to ExB drifts $v_{pol,ExB}$, other term such as ∇B drift velocity and impurity diffusion are less important so that we can write:

$$v_{pol,I} = \frac{B_{pol}}{B} v_{||,I} + v_{pol,ExB} \quad [3]$$

An example of the poloidal velocity for the neon case is shown in fig. 13 and the difference between $v_{pol,I}$ and $\frac{B_{pol}}{B} v_{||,I}$ represents the correction given by plasma drifts. Note that drifts affect the impurity poloidal velocity in two ways: through their contribution to $v_{||,i}$ and

through $v_{pol,ExB}$ indicating the importance of including drifts in the simulations to capture the impurity dynamics.

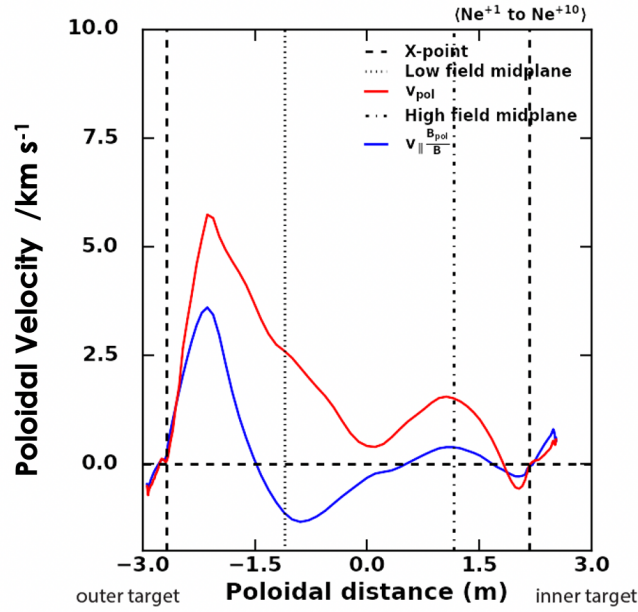


Figure 13: Poloidal velocity in red and $\frac{B_{pol}}{B} v_{||,i}$ in blue for the neon case (Ne^{+1} to Ne^{+10}). The difference between the two curves represents the contribution of $v_{pol,ExB}$.

Another important mechanism influencing the impurity leakage is the occurrence of flow reversal which takes place in a flux tube where the ionization source exceeds the ion loss to the target [31]. Since the SAS geometry leads to a strong localized ionization source [18], particle conservation requires that ions flowing into the divertor reverse their flow. Here flow reversal is found for both main ions and impurities as shown in fig. 14. Fig. 14a depicts the poloidal flow of the main ions in the neon case while the neon poloidal flow is shown in fig. 14b. The red color in figure 14 indicates clockwise flow away from the outer target while the blue color indicates counterclockwise direction towards the outer target. The white color corresponds to a region of stagnant flow. The figure demonstrates that the impurity flow is directed upstream not only where the main flow is already directed upstream but also in the regions where the thermal force is strong enough to counter balance the main ion flux directed towards the target. This result is important because in these flow reversal regions all the forces are directed upstream and the impurity leaks.

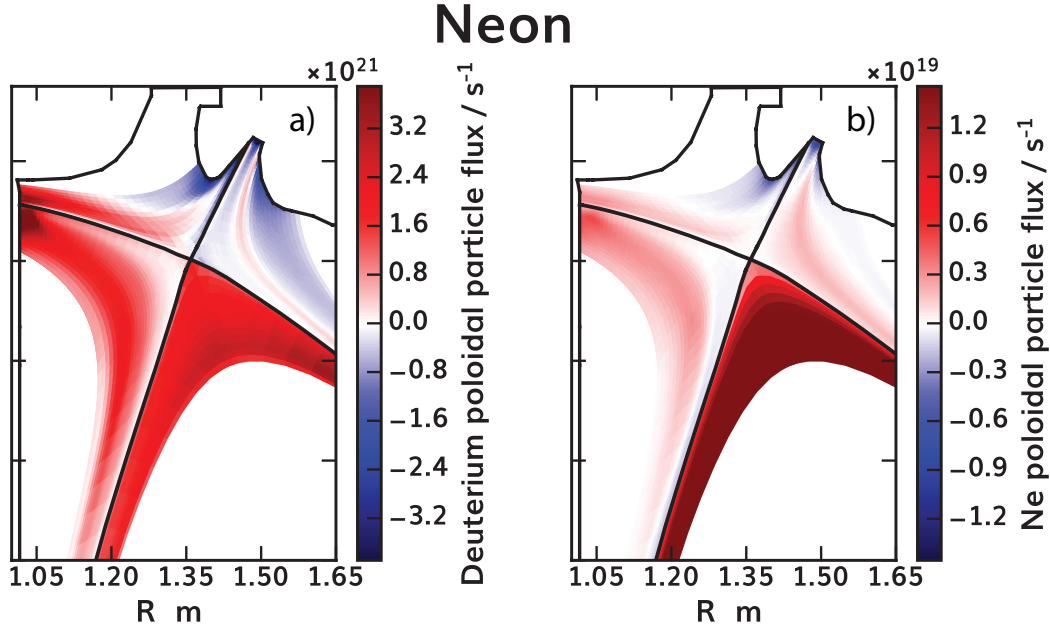


Figure 14: a) Main ions poloidal flow, b) Impurity poloidal flow for the neon case. The red color indicates clockwise flow away from the outer target while the blue color indicates counterclockwise direction towards the outer target. The white color corresponds to a region of stagnant flow.

The leakage efficiency of impurities finally depends on their ionization potential. For neon, both its high ionization potential and the effect of the shift in the stagnation due to the thermal force point in the direction of higher leakage. In the case of nitrogen, the increase leakage efficiency due to the thermal force competes with the ionization rate of nitrogen which enables nitrogen to ionize closer to the target than the deuterium neutrals. In general, nitrogen is ionized below the stagnation point of the poloidal flow and is retained. However, as discussed below, the final result depends on the divertor regime and the role of the drifts. Therefore, details of the transport can be evaluated only by numerical calculations.

The ionization strength of the main ions in the nitrogen seeded case is shown in fig. 15a, the ionization strength from neutral to first ionization state for the N is depicted in fig. 15b and the impurity poloidal flow for the N case is illustrated in fig. 15c. The ionization source of nitrogen is located just below the ionization source of deuterium and below the flow reversal regions in the outer divertor. Although a fraction of nitrogen neutrals can still reach the stagnation point and leak out of the outer target, nitrogen is mostly retained. It is worth noting that the nitrogen case is detached and the ionization front is peeling away from the target (red). Regions of strong recombination arise near the target (blue) indicating that very low temperature $T_e < 1$ eV has been achieved. Fig. 15 also demonstrate how the slot structure helps keeping the ionization source closer to the outer target reducing the probability of leakage from the divertor through the space between the plasma and the wall. Instead, in the inner leg where no baffling structure exists, leakage through the vacuum region can occur. The effect of drifts which shift the recycling source radially towards the inner target is also well visible in the 2D contour plot indicating the important role of convection.

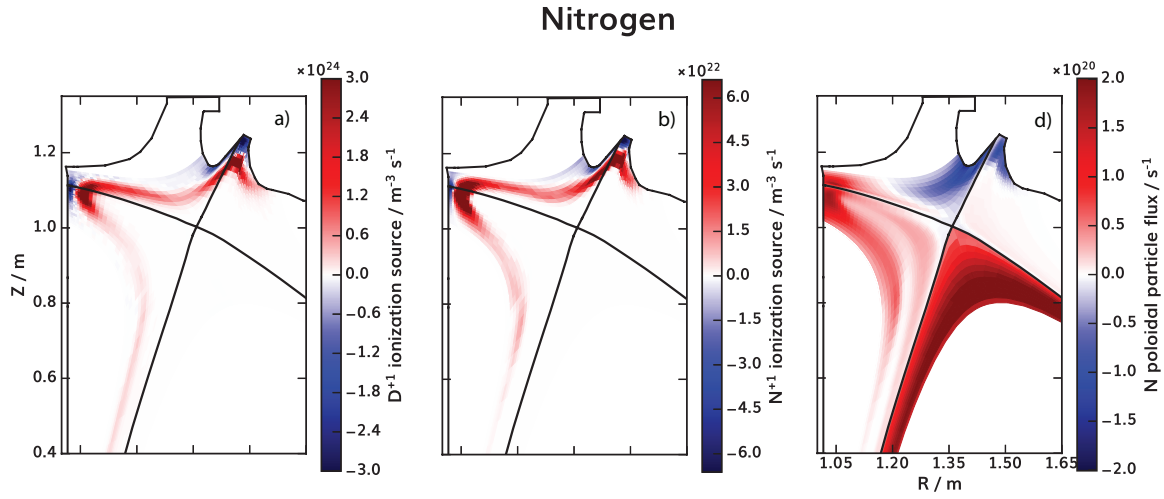


Figure 15: a) Ionization source strength for the main ions in the nitrogen case, b) Ionization source strength from neutral to first ionization state for nitrogen case, c) Main ions poloidal flow, c) Nitrogen poloidal flow. The red color indicates clockwise flow away from the outer target while the blue color indicates counterclockwise direction towards the outer target. The white color corresponds to a region of stagnant flow.

Note that the retention of nitrogen in the divertor can be also seen in the 2D contour plot of the impurity density (fig. 5a) where the zone with higher impurity density (in yellow) is concentrated at the outer target. Similarly, neon leakage is also visible in the 2D contour plot of the impurity density (fig. 5b) where no much neon is found at the outer target in the divertor (see green and yellow regions in fig. 5b).

3.3 IMPURITY ENRICHMENT FACTORS

Finally, an important figure of merit to characterize how effectively impurities are retained in the divertor is the impurity enrichment η . We calculated the impurity enrichment in the divertor as the ratio of the concentration at the divertor to concentration to the midplane:

$$\left(\frac{n_{z,d}}{n_{e,d}}\right) / \left(\frac{n_{z,m}}{n_{e,m}}\right) = \eta \quad [4]$$

where $n_{z,d}$ is the impurity density at the strike point divertor target, $n_{e,d}$ is the electron density at the divertor target, $n_{z,m}$ is the impurity density at outer midplane separatrix and $n_{e,m}$ is the electron density at the outer midplane separatrix. The calculated impurity enrichment is 0.32 for N and 0.16 for neon. The lower enrichment found for neon is consistent with the results above that neon leaks more efficiently out of the divertor. This is not only due to the higher ionization potential effect, but also to the fact that the mean free path for neutral impurities is longer for neon compared to nitrogen. This leads to a higher fraction of impurity neutrals ionizing in the core rather than in the divertor, thus increasing the impurity content in the

confined region and a lower content of the impurity in the divertor which is well consistent with the measured Ne emission illustrated in fig.3 and the experimental impurity density profiles shown in fig. 4.

In addition to the extrinsic impurities, carbon is an intrinsic radiator at DIII-D and in this paper we have demonstrated the different role of carbon in the N vs Ne seeded cases both in the experiments and in the numerical modeling. In order to consider the carbon role in the enrichment, we have performed additional calculations of the enrichment factor including both the seeded impurity, i.e. nitrogen or neon and the intrinsic impurity, i.e. carbon. As such, we define two additional enrichment factors:

$$\left(\frac{n_{N,d} + n_{C,d}}{n_{e,d}}\right) / \left(\frac{n_{N,m} + n_{C,m}}{n_{e,m}}\right) = \eta_{N+C} \quad \left(\frac{n_{Ne,d} + n_{C,d}}{n_{e,d}}\right) / \left(\frac{n_{Ne,m} + n_{C,m}}{n_{e,m}}\right) = \eta_{Ne+C} \quad [5]$$

The results of these calculations provide an enrichment factor of $\eta_{N+C} = 0.61$ for the nitrogen case and $\eta_{Ne+C} = 2.65$ for the neon case. This indicates that the neon case has much higher carbon enrichment in the divertor compared to the nitrogen case. The carbon density in the divertor in the neon seeded case is double that of the carbon density in the divertor for nitrogen seeded, and the midplane carbon density is lower in the neon case. These results are well in agreement with figure 10 where we showed how the radiation fraction due to carbon in the divertor is much higher in the neon case. Additionally, these calculated enrichment factors are consistent with the experimental observations obtained by divertor spectroscopy (fig. 4) which demonstrates that the carbon line emission in the nitrogen case is reduced and nitrogen is displacing carbon as the dominant radiator.

The upstream dissipation obtained with neon and the consequent reduction of the ELM frequency discussed in paragraph 2 is particularly important in present devices with a tungsten divertor as AUG [19] since impurity flushing from the pedestal is reduced resulting in impurity accumulation. In future devices, the pedestal will feature higher temperature and lower density gradients and neon ions in the pedestal will be fully stripped so they cannot radiate. Those effects will likely reduce the impact on the pedestal characteristics widening the operation window for Ne seeding as radiative impurity. The results presented in this work are well in agreement with impurity seeding studies performed for AUG and ITER [29, 30, 32, 33]. Impurities with higher ionization potential leak more efficiently out of the divertor. It is worth mentioning that this dynamic is also sensitive to the operative divertor regime: the terms in the flow velocity equations may vary with changing in the plasma conditions and for instance approaching detachment, the increased electron density reduces the neutral ionization length. Putting together all the effects illustrated above, the results of this analysis show that the impurity distribution depends on the ionization potential, ionization source distribution, drifts and main ion flow profile with a particular role played by flow reversal.

4. SUMMARY AND DISCUSSION

For the first time, impurity seeding studies were performed in the SAS graphite divertor at DIII-D using nitrogen and neon as seeded species. In this work we presented results where

the divertor geometry was kept fixed and the gas species was changed keeping all the other parameters constant. This enabled a comparative study of nitrogen versus neon as radiative species and their effect on power dissipation and pedestal performance. The experimental results show that N remains compressed in the divertor, thereby providing high radiative losses without affecting the pedestal profiles and replacing the intrinsic C emission along the line of sight observed by the DivSPRED diagnostic along the outer SOL. Neon, instead radiates more upstream than N thus reducing the power flux through the separatrix leading to a reduced ELM frequency and compression in the divertor. Neon readily enters the pedestal causing an increase in the pedestal density gradient with a large neon density measured in the core. The different dissipative behaviour of the two impurities found in the experiments was confirmed by SOLPS-ITER modelling which for the first time at DIII-D includes multiple impurity species and a treatment of full drifts and currents. The impurity transport in the SOL was studied in detail in terms of the parallel momentum balance and poloidal flows. Consistent with its higher ionization potential and longer mean free path, nitrogen is better retained in the divertor compared to neon although a fraction of nitrogen neutrals can still reach the stagnation point. Since carbon is an intrinsic radiator at DIII-D, in this paper we have also demonstrated the different role of carbon in the N vs Ne seeded cases both in the experiments and in the numerical modeling. Carbon contributes more when neon seeding is injected compared to when nitrogen is used. In the N case, nitrogen is displacing carbon as the dominant radiator as showed by the reduction of the carbon line emissions measured by divertor spectroscopy and by the reduced carbon radiation fraction and enrichment factor as calculated by SOLPS-ITER.

While the suitability for power exhaust by an impurity depends on its radiative efficiency as a function of the temperature, it is important to emphasize that the understanding of the mechanism leading to impurity leakage requires a detailed study of the ionization potential, ionization source distribution, drifts and main ion flow profile. In the cases presented here, the highly localized ionization source due to the pronounced closure and target shaping of the SAS leads to a reversal of the plasma flow affecting the parallel momentum balance. Additionally, the presence of drifts, which in our SAS geometry cases are in the same order of amplitude as the recycling plasma flows, brings an additional significant correction to the poloidal stagnation point. As such, the results presented here are an important example of the impact of flow reversal and plasma drifts in a closed divertor structure with significant consequences on the SOL impurity transport and pedestal behavior.

This work also reinforces the argument that such effects are very pronounced in medium size tokamaks like DIII-D and AUG [29, 30, 31] due to the smaller size of the divertor compared to larger machines such as JET and ITER [32, 33]. In future large devices drifts still have important effect, though maybe not as dramatic. It is predicted that the impact on the pedestal in future machines will be reduced due to higher temperature gradients and the fact that both nitrogen and neon ions will be fully stripped. While the relative importance of the terms will change in future devices, advancing our understanding of the fundamental physics of divertor impurity leakage and the changes associated with SOL and pedestal characteristics in present devices is crucial to extrapolate to future devices. This work strongly contributes to such effort through both experiments and modeling supporting the importance of analyzing the effects of drifts and flows for SOL impurity transport and expanding the physics understanding of the leakage mechanism into a closed divertor configuration where closure and target shaping play an important role into the underlying mechanism.

ACKNOWLEDGEMENTS

This material is based upon work supported by the U.S. Department of Energy, Office of Science, Office of Fusion Energy Sciences, using the DIII-D National Fusion Facility, a DOE Office of Science user facility, under Award Nos. DE-FC02-04ER54698 (DIII-D), DE-AC52-07NA27344 (LLNL), DE-AC02-09CH11466 (PPPL).

Disclaimer: This report was prepared as an account of work sponsored by an agency of the United States Government. Neither the United States Government nor any agency thereof, nor any of their employees, makes any warranty, express or implied, or assumes any legal liability or responsibility for the accuracy, completeness, or usefulness of any information, apparatus, product, or process disclosed, or represents that its use would not infringe privately owned rights. Reference herein to any specific commercial product, process, or service by trade name, trademark, manufacturer, or otherwise does not necessarily constitute or imply its endorsement, recommendation.

REFERENCES

- [1] A. KALLENBACH, M. BERNERT, M. BEURSKENS, L. CASALI, M. DUNNE, T. EICH, L. GIANNONE, A. HERRMANN, M. MARASCHEK, S. POTZEL et al., *Nucl. Fusion* 55, 053026 (2015)
- [2] M.E. FENSTERMACHER, J. BOEDO, R.C. ISLER, A.W. LEONARD, G.D. PORTER, D.G. WHYTE, R.D. WOOD, S.L. ALLEN, N.H. BROOKS, R. COLCHIN et al., *Plasma Phys. Controlled Fusion* 41, A345–A355 (1999)
- [3] A. LOARTE, *Plasma Phys. Controlled Fusion* 43, R183–R224 (2001)
- [4] B. LIPSCHULTZ, B. LABOMBARD, J.L. TERRY, C. BOSWELL, and I.H. HUTCHINSON, *Fusion Sci. Technol.* 51(3), 369–389 (2007)
- [5] L. CASALI, C. SANG, A. MOSER, B. COVELE, H. GUO, AND C. SAMUELL, *Contrib. Plasma Phys.* 58(7–8), 725–731 (2018)
- [6] R. NEU, J.C. FUCHS, A. KALLENBACH, C. MAGGI, V. ROHDE, F. RYTER, T. EICH, J. GAFERT, O. GRUBER, G. HAAS et al., *Nucl. Fusion* 43, 1191–1196 (2003)
- [7] C. GIROUD, S. JACHMICH, P. JACQUET, A. JAERVINEN, E. LERCHE, F. RIMINI, L. AHO-MANTILA, N. AIBA, I. BALBOA, P. BELO *Plasma Phys. Controlled Fusion* 57 035004 (2015)
- [8] N. ASAKURA, T. NAKANO, N. OYAMA, T. SAKAMOTO, G. MATSUNGA, K. ITAMI *Nucl. Fusion* 49 115010 (2009)
- [9] A. MOSER L. CASALI, B.M. COVELE, A.W. LEONARD, A.G. MCLEAN, M.W. SHAFER, H.Q. WANG, and J.G. WATKINS, *Phys. Plasmas* 27, 032506 (2020)
- [10] C. GIROUD, S. BREZINSEK, R. PITTS, A. HUBER, J. MAILLOUX, A. CHANKIN, E. KAVEEVA, S. HENDERSON, J. HILLESHEIM, E. LERCHE et al. “High performance ITER-baseline discharges in deuterium with nitrogen and neon seeding in the JET-ILW” *Proc. Int. Conf. 28th IAEA Fusion Energy Conference (FEC 2020) Nice, France 10-15 May 2021*
- [11] C. GIROUD, G. MADDISON, S. JACHMICH, F. RIMINI, M. BEURSKENS, I. BALBOA, S. BREZINSEK, R. COELHO, J. COENEN L. FRASSINETTI et al. *Nucl. Fusion* 53 113025 (2013)
- [12] A. KALLENBACH, M. BERNERT, R. DUX, L. CASALI, T. EICH, L. GIANNONE, A. HERMANN, R. MCDERMOTT, A. MLYNEK, H.W. MUELLER et al., *Plasma Phys. Controlled Fusion* 55, 124041 (2013)
- [13] L. CASALI, M. BERNERT, R. DUX, R. FISCHER, A. KALLENBACH, B. KURZAN, P. LANG, A. MLYNEK, R. M. MCDERMOTT, F. RYTER et al., *EPJ Web Conf.* 79, 01007 (2014)
- [14] H.D. PACHER, A. KUKUSHKIN, G.W. PACHER, V. KOTOV, G. JANESCHITZ, D. REITER and D. COSTER, *J. Nucl. Mater.* 390–391, 259–262 (2009)
- [15] A. KUKUSHKIN, H. PACHER, G. JANESCHITZ, A. LOARTE, D. COSTER, G. MATTHEWS, D. REITER, R. SCHNEIDER, AND V. ZHOGOLEV, *Nucl. Fusion* 42, 187 (2002)
- [16] L. CASALI, B.M. COVELE AND H.Y. GUO *Nucl. Mater. Energy* 19 537–43 (2019)
- [17] H.Y. GUO, H.W. WANG, J.G. WATKINS, L. CASALI, B. COVELE, A. L. MOSER, T. OSBORNE, C.M. SAMUELL, M.W. SHAFER, P.C. STANGEBY et al., *Nucl. Fusion* 59, 086054 (2019)
- [18] L. CASALI, T.H. OSBORNE, B.A. GRIERSON, A.G. MCLEAN, E.T. MEIER, J. REN, M.W. SHAFER, H. WANG and J.G. WATKINS *Phys. Plasmas* 27, 062506 (2020)
- [19] M. BERNERT, M. WISCHMEIER, A. HUBER, F. REIMOLD, B. LIPSCHULTZ, S. BREZINSEK, R. DUX, T. EICH, KALLENBACH, A. LEBSCHY et al. *Nucl. Mater. Energy* 12, 111-118 (2017)
- [20] G. MADDISON, C. GIROUD, G. McCORMICK, J. ALONSO, B. ALPER. G. ARNOUX, P. DA SILVA ARESTA BELO, M. BEURSKENS, A BOBOC, S. BREZINSEK ET AL. “Moderation of divertor heat load by fueling and impurity seeding in well-confined ELMY H-mode plasma on JET”. *Nucl. Fusion* 51 042001 (2011)

- [21] X. BONNIN, W. DEKEYSER, R. PITTS, D. COSTER, S. VOSKOBOYNIKOV, AND S. WIESEN, *Plasma Phys. Controlled Fusion* 11, 1403102 (2016)
- [22] E. SYTOVA, E. KAVEEVA, V. ROZHANSKY, I. SENICHENKOV, S. VOSKOBOYNIKOV, D. COSTER, X. BONNIN, AND R. PITTS, *Contrib. Plasma Phys.* 58(6–8), 622–628 (2018)
- [23] E. T. MEIER, R. GOLDTON E. KAVEEVA M. MAKOWSKI, S MORDIJCK, V. ROZHANSKY, SENICHENKOV, I., S. VOSKOBOYNIKOV *Nucl. Mater. Energy* 12, 973 (2017)
- [24] S.TOUCHARD, J. MOUGENOT, C. ROND. K. HASSOUNI, X. BONNIN *Nuclear Materials and Energy* 18 12-17 (2019)
- [25] W. ECKSTEIN AND J. BIERSACK *NUCL. INSTRUM. METHODS PHYS. RES. B2* 2,550-554 (1984)
- [26] J. BOHDANSKY AND J. ROTH 1980 *J. PHYS.* 51 2861
- [27] J. NICHOLS, T. ABRAMS, C. CHROBAK, D. DONOVAN, J. DURAN, J. ELDER, D. RUDAKOV, P. STANGEBY, E. UNTERBERG, W. WAMPLER ET AL. *Nucl. Fusion* 61 096018 (2021)
- [28] L. CASALI, E. FABLE, R. DUX, F. RYTER, and ASDEX Upgrade Team, *Phys. Plasmas* 25, 032506 (2018)
- [29] E. SYTOVA, R. PITTS, E. KAVEEVA, X. BONNIN, D. COSTER, D. COSTER, V. ROZHANSKY, I. SENICHENKOV, I. VESELOVA, S. VOSKOBOYNIKOV, AND F. REIMOLD, *Nucl. Mater. Energy* 19, 72–78 (2019)
- [30] I. SENICHENKOV, E. KAVEEVA, E. SYTOVA, V. ROZHANSKY, S. VOSKOBOYNIKOV, I. VESELOVA, D. COSTER, X. BONNIN, F. REIMOLD, and ASDEX-Upgrade Team, *Plasma Phys. Controlled Fusion* 61, 045013 (2019)
- [31] L. CASALI, D. ELDON, J.A. BOEDO, T. LEONARD, B. COVELE, *Nucl. Fusion* 60, 076011 (2020)
- [32] V. ROZHANSKY, E. KAVEEVA, I. SENICHENKOV, I. VESELOVA, S. VOSKOBOYNIKOV, R. PITTS, S. WIESEN, C. GIROUD, D. COSTER “Multi-machine SOLPS-ITER comparison of impurity seeded H- mode radiative divertor regimes with metal walls” *Proc. Int. Conf. 28th IAEA Fusion Energy Conference (FEC 2020) Nice, France 10-15 May 2021*
- [33] E. KAVEEVA, V. ROZHANSKY, I. VESELOVA, I. SENICHENKOV, C. GIROUD, R. PITTS, S. WIESEN, S. VOSKOBOYNIKOV *Nuclear Materials and Energy* 28 101030 (2021)